

advances.sciencemag.org/cgi/content/full/6/16/eaaz0906/DC1

Supplementary Materials for

Exceptional capacitive deionization rate and capacity by block copolymer–based porous carbon fibers

Tianyu Liu, Joel Serrano, John Elliott, Xiaozhou Yang, William Cathcart, Zixuan Wang, Zhen He, Guoliang Liu*

*Corresponding author. Email: gliu1@vt.edu

Published 17 April 2020, *Sci. Adv.* **6**, eaaz0906 (2020)
DOI: 10.1126/sciadv.aaz0906

This PDF file includes:

Supplementary Methods

Figs. S1 to S8

Tables S1 and S2

References

1. Supplementary Methods

1.1 Desalination capacity

The desalination capacity, Γ (in $\text{mg}_{\text{salt}} \text{ g}^{-1}_{\text{electrode}}$), was determined by the change in salt concentration before and after desalination, according to the following equation,

$$\Gamma = \frac{(C_0 - C_t) \cdot V}{m} \quad (\text{S1})$$

where C_0 and C_t represent the initial and final solution concentrations, respectively, and are converted from electrical conductivities using the calibration curves (Supplementary Figure 8); V is the volume of salt solutions (20 mL); m is the total mass of the active materials loaded on two electrodes (~ 15 mg).

1.2 Average desalination rate

The average desalination rate, v (in $\text{mg}_{\text{salt}} \text{ g}^{-1}_{\text{electrode}} \text{ min}^{-1}$), was evaluated by the following equation,

$$v = \frac{\Gamma}{t} \quad (\text{S2})$$

where t is the charging time (min).

1.3 Electrical conductivity

The electrical conductivity (S , in S cm^{-1}) was derived from sheet resistance (R_s , in Ω/\square) measured by a four-point probe conductivity meter according to the following equation,

$$S = \frac{1}{R_s \cdot d} \quad (\text{S3})$$

where d is film thickness (cm).

1.4 Surface area

The effective surface area (A_{eff}) for desalination was estimated according to Equation S4, assuming that Na^+ ions form a monolayer on electrode surfaces and the desalination capacity is exclusively contributed by electrical double layers,

$$A_{\text{eff}} = \frac{\pi r_{\text{Na}^+}^2 \cdot \Gamma \cdot N_A}{M_{\text{NaCl}}} \quad (\text{S4})$$

where r_{Na^+} is the radius of hydrated Na^+ (360 nm); N_A is Avogadro number ($6.02 \times 10^{23} \text{ mol}^{-1}$); M_{NaCl} is the molecular weight of NaCl (58.4 g mol^{-1}).

1.5 Diffusion coefficient

According to Qu *et al.*(49), the Na^+ diffusion coefficient (D_{Na^+} , in $\text{cm}^2 \text{ s}^{-1}$) was estimated by the following Warburg impedance equation of electrolyte-flooded (electrodes immersed in a large amount of electrolyte) electrochemical systems (*e.g.*, CDI cells),

$$D_{\text{Na}^+} = \frac{1}{2} \left(\frac{RT}{F^2 c \sigma A} \right)^2 \quad (\text{S5})$$

where R is gas constant ($8.314 \text{ J K}^{-1} \text{ mol}^{-1}$); T is temperature (298.15 K); F is Faraday constant (96485 C mol^{-1}); c is Na^+ concentration in bulk electrolytes ($8.56 \times 10^{-6} \text{ mol cm}^{-3}$); σ is diffusion resistance (in $\Omega \text{ s}^{-0.5}$) obtained by fitting Nyquist plots (fig. S3, B-D); A is the electrode geometric area (9.5 cm^2).

1.6 Coulombic efficiency

Coulombic efficiency (CE%) equals the ratio of charges used for ion adsorption to the total charges flowed into CDI cells,

$$D_{\text{Na}^+} = \frac{1}{2} \left(\frac{RT}{F^2 c \sigma A} \right)^2 \quad (\text{S5})$$

where R is gas constant ($8.314 \text{ J K}^{-1} \text{ mol}^{-1}$); T is temperature (298.15 K); F is Faraday constant (96485 C mol^{-1}); c is Na^+ concentration in bulk electrolytes ($8.56 \times 10^{-6} \text{ mol cm}^{-3}$); σ is diffusion resistance (in $\Omega \text{ s}^{-0.5}$) obtained by fitting Nyquist plots (fig. S3, B-D); A is the electrode geometric area (9.5 cm^2).

1.6 Coulombic efficiency

Coulombic efficiency (CE%) equals the ratio of charges used for ion adsorption to the total charges flowed into CDI cells,

$$\text{CE\%} = \left(\frac{\Gamma_F}{M_{\text{NaCl}}} \right) / \left(\int_0^t I dt \right) \quad (\text{S6})$$

where I and t represent the charging current (in A g⁻¹) and charging time (in s), respectively. Typical CE% of a CDI cell without any ion-exchange membranes is in the range of 0.5 – 0.8 (50).

1.7 Energy normalized adsorbed salt (ENAS)

For constant-voltage CDI (zero discharge voltage), the energy normalized adsorbed salt (ENAS) is calculated according to the following equation:

$$\text{ENAS} = \frac{\Gamma}{E_{\text{in}}} = \frac{\Gamma}{U \int_0^{t_C} I_C dt} \quad (\text{S7})$$

where Γ , E_{in} , U , t_C , and I_C represent desalination capacity (in mg_{NaCl} g_{PCF}⁻¹), energy input during charging (in J g_{PCF}⁻¹), applied voltage (in V), charging time (in s), and charging current density (in A g_{PCF}⁻¹), respectively.

2. Supplementary Figures

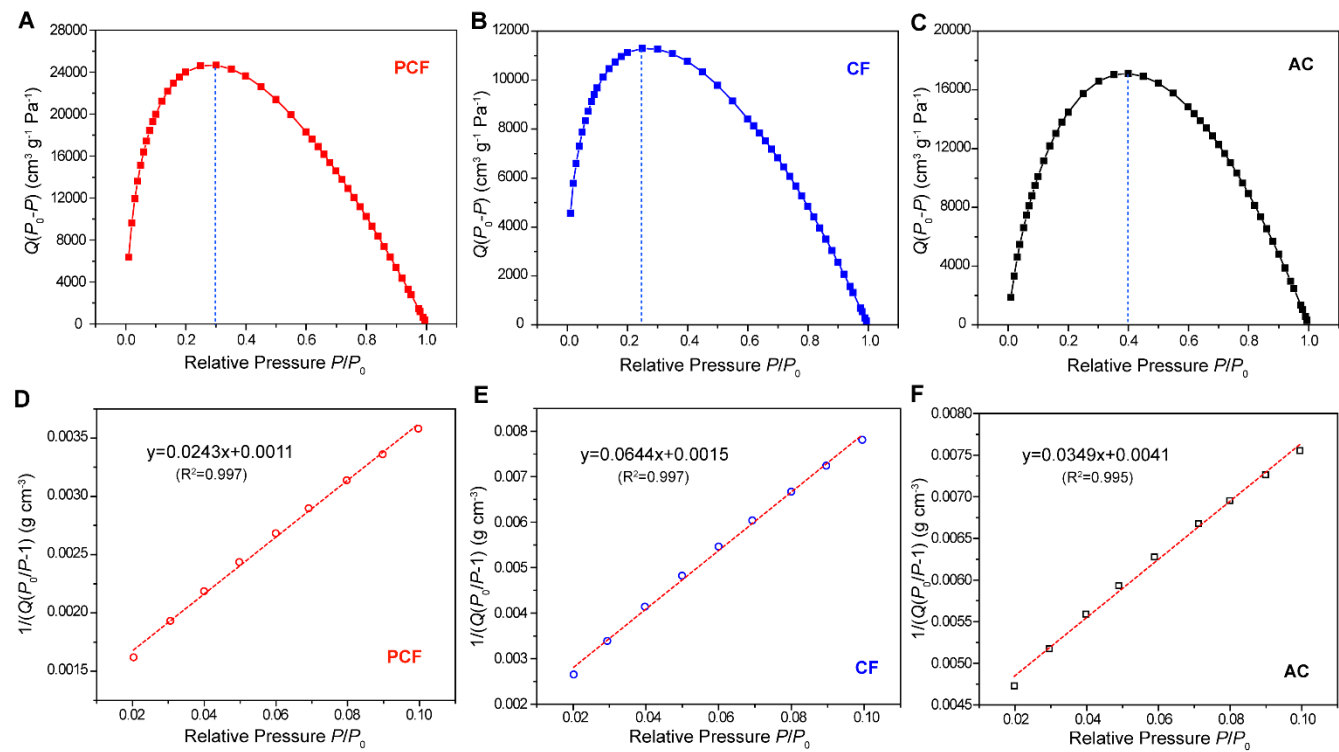


Fig. S1. Validation of the CO₂ BET Surface Areas. (A-C) $Q(P_0 - P)$ versus relative pressure of CO₂ during the sorption on (A) PCF, (B) CF and (C) AC. The dashed lines mark the peak positions. (D-F) BET plots of (D) PCF, (E) CF and (F) AC. Q , P_0 , and P are gas adsorption quantity (cm³ g⁻¹), saturation pressure (760 mmHg), and gas pressure (mmHg), respectively.

The CO₂-based BET surface areas were lower than the N₂-based BET surface areas, because a higher operating temperature (273 K for CO₂ vs. 77 K for N₂) leads to a smaller quantity of adsorbed gas molecules at adsorption-desorption equilibria (51). By analyzing the relationships between gas adsorption quantity and relative pressure (fig. S1), as proposed by Kim *et al.* (52), the CO₂-based BET surface areas were validated, because the following conditions are met:

- 1) The linear relative pressure range in the BET plots (fig. S1, D-F) must correspond to positive slope in the $Q(P_0 - P)$ vs. relative pressure plots (fig. S1, A-C, the section to the left of the dashed lines);
- 2) The y-intercepts of the linear lines in the BET plots (fig. S1, D-F) must be positive.

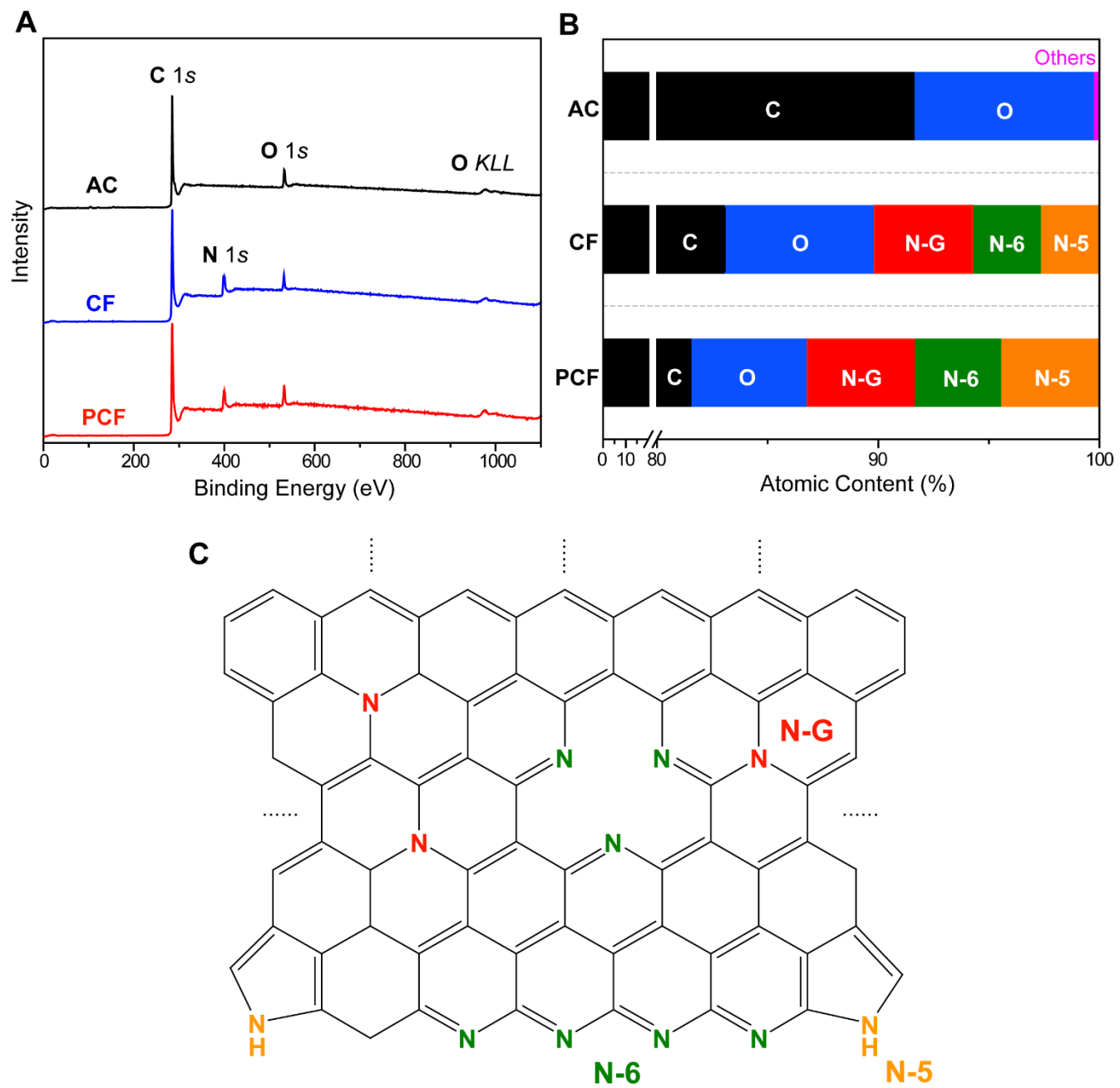


Fig. S2. Elemental compositions of PCF, CF, and AC. (A) XPS survey spectra. (B) Atomic contents. In AC, “Others” include Mg and Si. (C) Schematic of a possible configuration of nitrogen dopants. N-G: graphitic-N; N-6: pyridinic-N; N-5: pyrrolic-N.

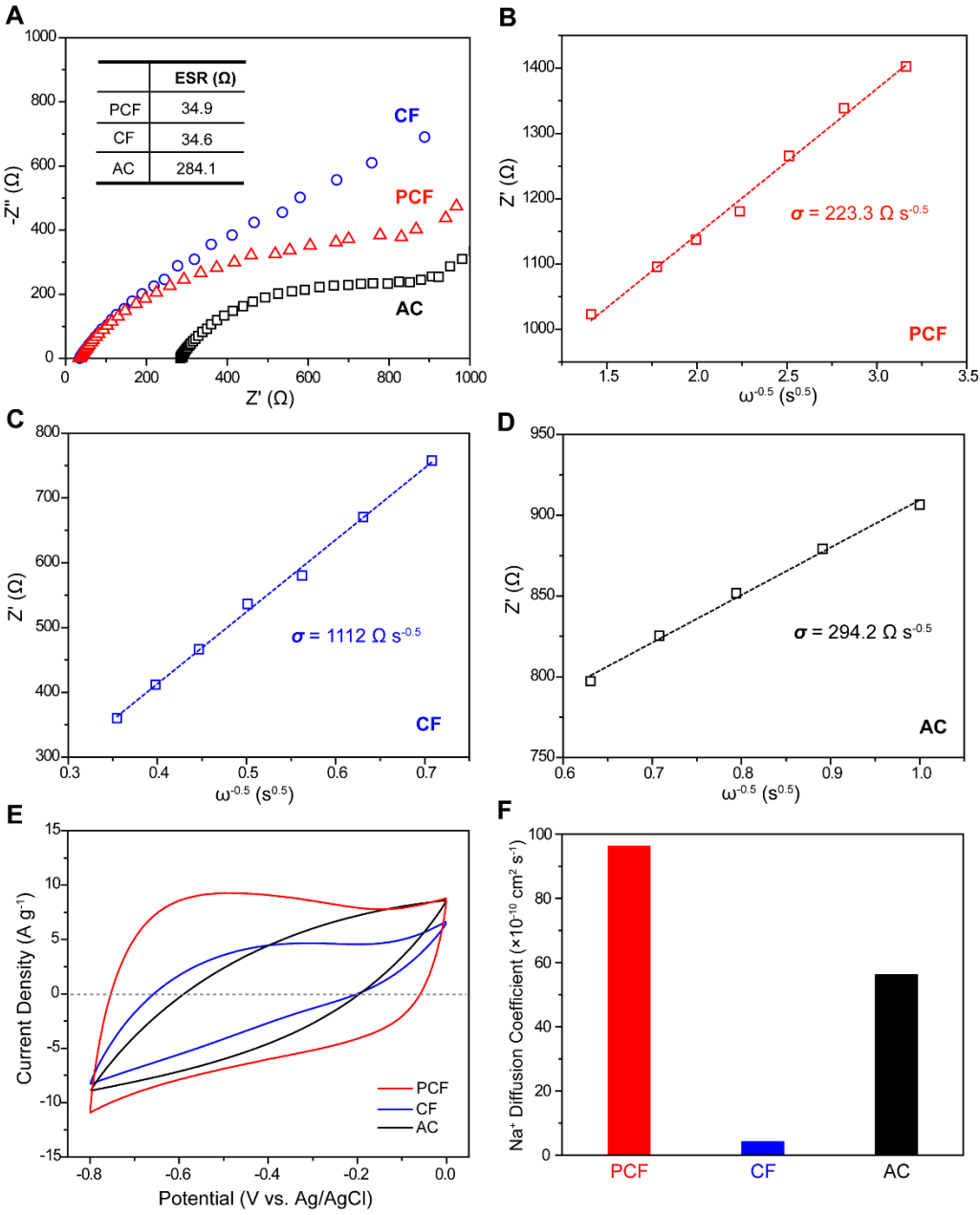


Fig. S3. Additional electrochemical performances. (A) Nyquist plots of the PCF, CF, and AC desalination cells containing 500 mg L⁻¹ of NaCl solutions. The inset table lists the electrical series resistance (ESR) values. (B-D) Z' vs. reciprocal of the square root of frequency (ω) for (B) PCF, (C) CF, and (D) AC. The dashed lines are the linear best fittings, the slopes of which equal to the diffusion resistances (σ) of the ions in the carbon materials. (E) Cyclic voltammograms of PCF, CF, and AC at 100 mV s⁻¹ in 2000 mg L⁻¹ NaCl aqueous solutions. (F) Diffusion coefficients of Na⁺ in PCF, CF, and AC probed by EIS in 500 mg L⁻¹ NaCl solutions.

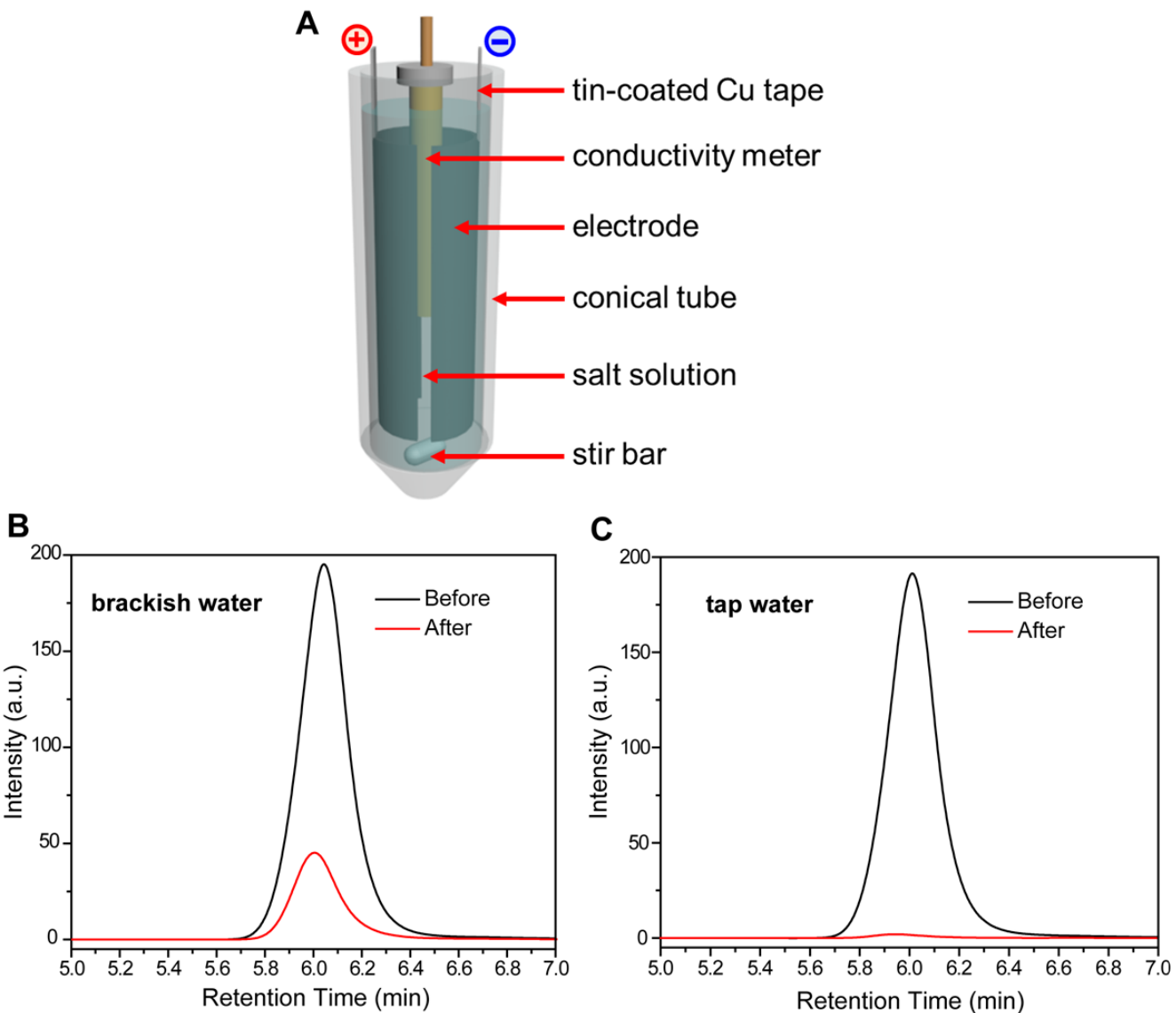


Fig. S4. Cell configuration and ion chromatography. (A) Schematic illustration of a deionization cell composed of two carbon electrodes adhered to Sn tapes and a conductivity meter enclosed in a conical tube. A stir bar was used to keep the salt concentration homogenous in the solution for measurement purposes. The cell contained an excess of NaCl solution to probe the intrinsic deionization properties of PCF. (B and C) Representative Cl^- ion chromatograms of (B) brackish water and (C) tap water before and after deionization.

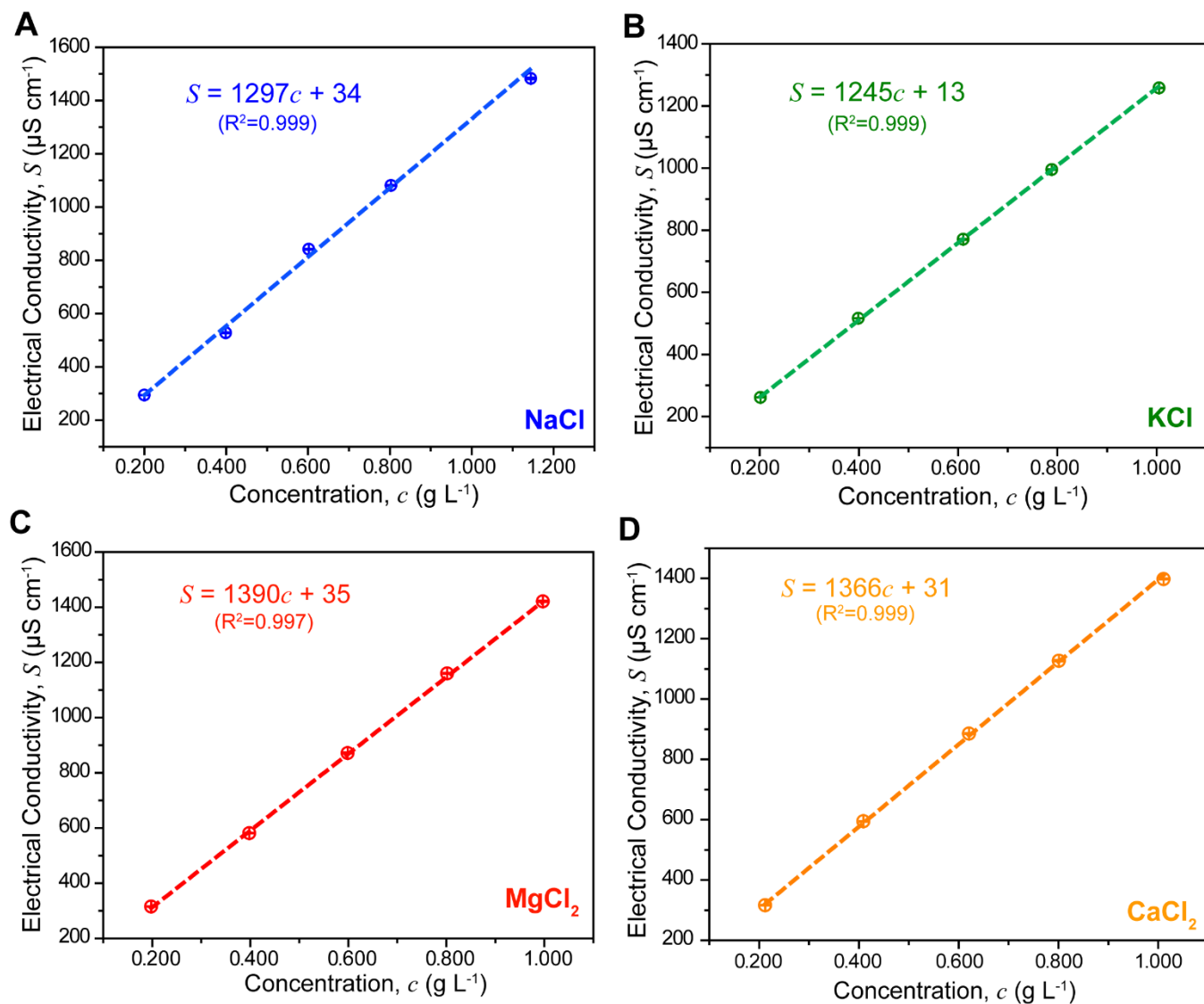


Fig. S5. Calibration curves of (A) NaCl, (B) KCl, (C) MgCl₂, and (D) CaCl₂ aqueous solutions. Each data point represents the average ionic conductivity of five independent measurements. The dashed lines are the best linear fittings.

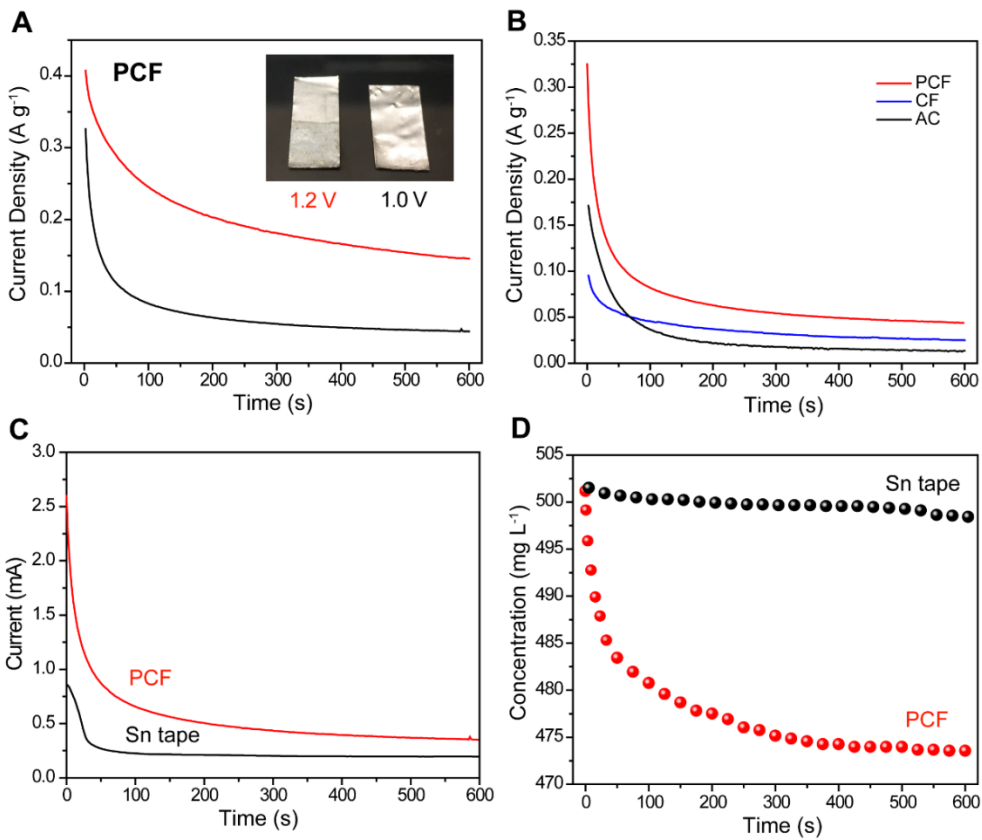


Fig. S6. Electrochemical properties. All materials were tested in 500 mg L^{-1} NaCl aqueous solutions.

(A) Constant-voltage charge-discharge profiles of PCF at 1.0 V (black) and 1.2 V (red). Inset: Photograph of bare tin tapes charged at 1.2 V and 1.0 V for 600 s. (B) Current density (normalized to the mass of active material) time-evolution profiles of PCF, CF, and AC during charging (1.0 V). (C) Current and (D) NaCl concentration *vs.* time for the desalination cells with two symmetric electrodes of PCF on Sn tapes (red) and bare Sn tapes (black). The applied bias was 1.0 V for both electrodes. The cells contained an excess of NaCl solution (500 mg L^{-1}) to probe the intrinsic deionization properties of the materials.

By integrating the areas below the charging curves (fig. S6B), we estimated the Coulombic efficiencies of PCF, CF, and AC to be 0.72, 0.85, and 0.47, respectively, using Equation S6. The appreciably lower Coulombic efficiency of AC could originate from its high internal resistance, as reflected by its limited electrical conductivity. The limited electrical conductivity induced charge dissipation and resulted in inefficient charge utilization.

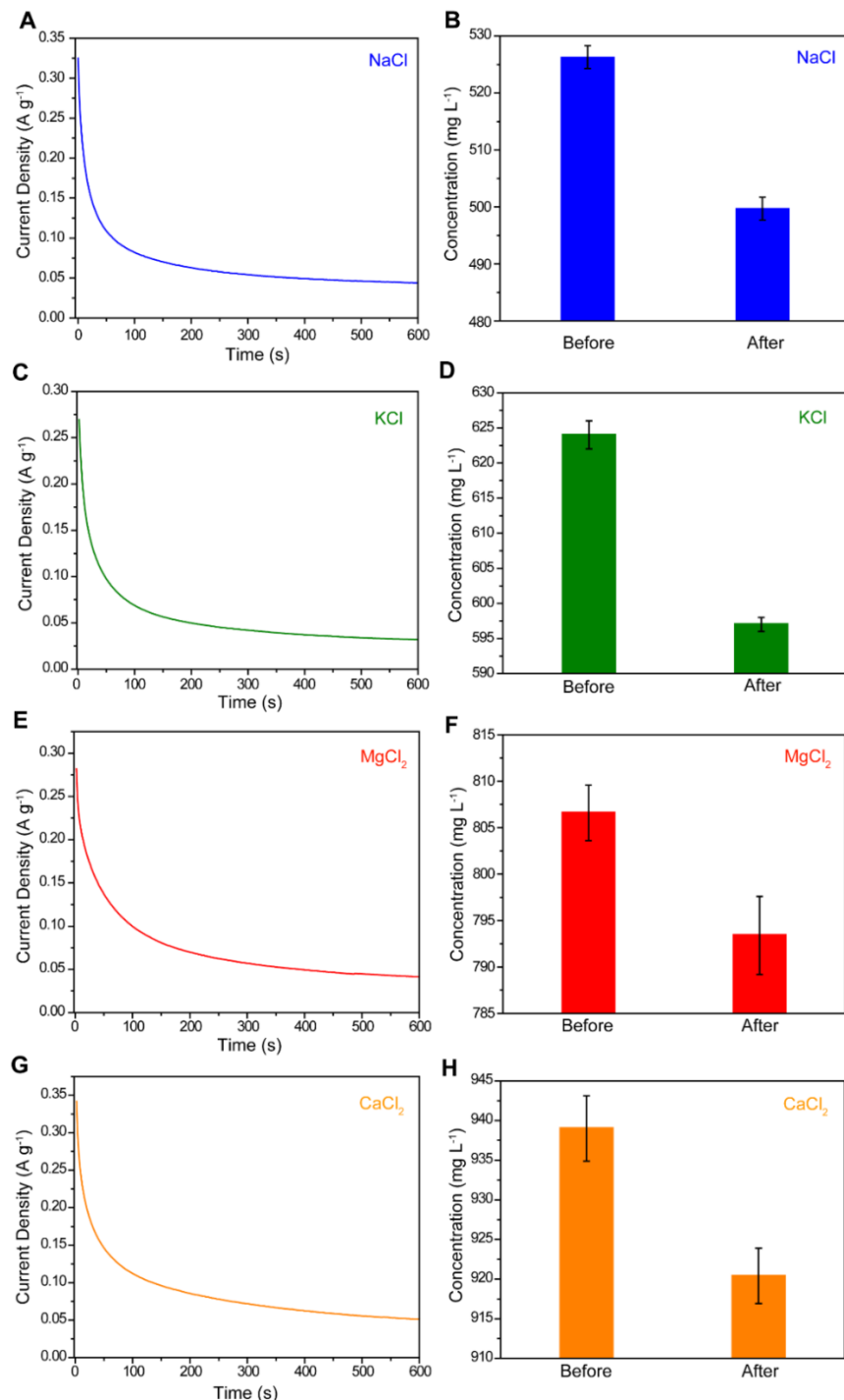


Fig. S7. Constant-voltage deionization performances of PCF. (A, C, E, and G) The current density (based on the mass of active material) time-evolution profiles of charging PCF in (A) NaCl , (C) KCl , (E) MgCl_2 , and (G) CaCl_2 aqueous solutions. (B, D, F, H) Bar charts of (B) NaCl , (D) KCl , (E) MgCl_2 and (H) CaCl_2 concentrations before and after desalination. The error bars represent one standard deviation.

To probe the influence of block copolymer molecular weight and composition, a new batch of PCF (PCF-n) from PMMA-*b*-PAN with a molecular weight of 63-*b*-107 kDa ($\phi_{\text{PAN}} \sim 0.61$, polydispersity=1.12) was prepared. The original PCF was from PMMA-*b*-PAN with a molecular weight of 48-*b*-52 KDa ($\phi_{\text{PAN}} \sim 0.52$, polydispersity=1.08). N₂- and CO₂-physisorption both revealed that the surface areas of PCF-n were appreciably lower than those of PCF (fig. S8, A-C). The lower surface areas corroborated with our recent finding that PCF from PMMA-*b*-PAN of $\phi_{\text{PAN}} \sim 0.5$ showed the highest surface areas (43). Due to the decreased surface area, the desalination capacity of PCF-n was $11.5 \pm 1.8 \text{ mg g}^{-1}$, ~38% of that of PCF measured in 500 mg L⁻¹ NaCl aqueous solutions (fig. S8D). This result demonstrated a positive correlation between the desalination capacity and surface area of PCF. The latter depended strongly on the molecular weight and composition of PMMA-*b*-PAN.

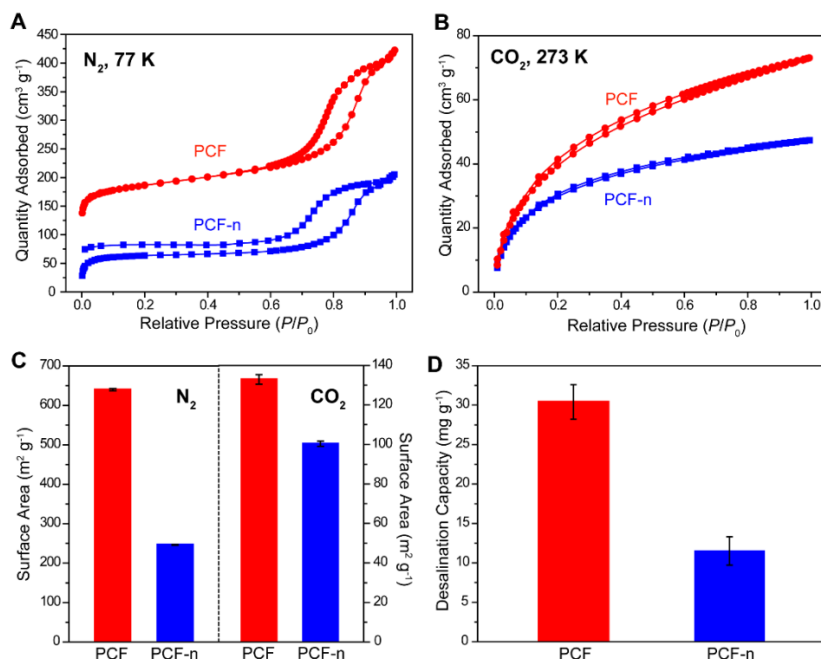


Fig. S8. Effects of block copolymer molecular weight and composition on PCF. (a) N₂ physisorption isotherm at 77 K and (b) CO₂ physisorption isotherms at 273 K. (C) Surface areas of PCF and PCF-n. The error bars are systematic errors of the instrument. (D) Desalination capacities of PCF and PCF-n (charging voltage: 1.0 V; 500 mg L⁻¹ NaCl aqueous solutions). The error bars represent one standard deviation.

3. Supplementary Tables

Table S1. NaCl concentrations of brackish water (BW) and tap water (TW) before and after deionization.

Batch	Initial Concentration		Final Concentration	
	(mg L ⁻¹)		(mg L ⁻¹)	
	Cl ⁻	NaCl ^{a)}	Cl ⁻	NaCl ^{a)}
BW#1	60.1	990	13.5	223
BW#2	60.4	996	13.4	221
BW#3	60.6	999	13.0	214
BW#4	58.9	971	14.5	239
TW#1	57.6	475	0.61	5.0
TW#2	57.2	472	0.55	4.5
TW#3	57.4	473	0.63	5.2
TW#4	57.1	471	0.89	7.3

Note:

a) The NaCl concentrations (c_{NaCl}) were evaluated based on the Cl⁻ concentration (c_{Cl^-}) measured by ion chromatography,

$$c_{\text{NaCl}} = \text{DF} \times c_{\text{Cl}^-} \times \frac{M_{\text{NaCl}}}{M_{\text{Cl}^-}},$$

where M_{Cl^-} and M_{NaCl} are molar masses of Cl⁻ (35.45 g mol⁻¹) and NaCl (58.44 g mol⁻¹), respectively. DF is a diluting factor of the solutions injected into ion chromatograph columns to avoid detector saturation. For tap water, DF = 5; For brackish water, DF = 10.

Table S2. Capacitive desalination performances of selected state-of-the-art carbon-based electrodes.

[The data listed in this table are mainly selected from performances obtained with desalination conditions similar to our work: two-electrode system, no ion-exchange membranes, and desalination potentials <1.5 V. The data here are mainly for comparison of materials performance rather than engineering of the device design. This table by no means is exhaustive but represents the state-of-the-art for comparison.]

Electrode ^{a)}	NaCl Concentration (mg L ⁻¹)	Voltage (V)	Desalination Capacity (mg g ⁻¹ electrode)	Average Desalination Rate (mg g ⁻¹ electrode min ⁻¹)	Ref.
PCF	500	1.0	30.4	3.0-38	This work
CF	500	1.0	7.4	0.74	This work
AC	500	1.0	11.0	1.1	This work
Carbon Nanotubes					
CNT-CNF composite	500	1.2	16.3	0.51	(53)
CNT sponge	500	1.2	17.0	0.05	(54)
Single-walled CNT/porous reticulated vitreous carbon	75	1.1	3.2	0.64	(55)
Graphene/CNT hybrid sponge	500	1.2	18.7	0.62	(56)
CNT	500	1.2	2.5	~0.025	(57)
Carbon Fibers					
Electro-spun CNF	60	1.2	1.3	0.0013	(58)

ZnCl ₂ -activated CNF	500	1.2	10.5	0.17	(59)
Hollow CNFs	-	1.2	1.9	0.021	(60)
N-doped PAN-derived carbon nanofibers	585	1.2	19.9	3.98	(61)
Graphene coated, N-doped PAN-derived carbon nanofibers	585	1.2	27.6	1.84	(61)
N-doped porous carbon nanofiber aerogel	500	1.2	14.3	0.24	(62)
P-doped carbon nanofiber aerogel	1000	1.2	16.2	0.27	(63)
Cellulose-derived CNF	500	1.2	13.1	0.066	(64)

Graphene

N-doped nanoporous graphene aerogel	50	1.5	21	0.7	(24)
Nanoporous graphene aerogel	500	1.2	12.4	0.21	(65)
3D porous graphene aerogel	25	1.2	6.2	0.069	(66)
N-doped graphene powder	-	1.8	4.8	0.12	(67)

Graphene powder	-	1.8	3.9	0.098	(67)
N-doped graphene sponge	50	1.2	8.0	0.27	(24)
Graphene spheres	25	1.6	2.3	1.2	(68)
Graphene/mesoporous carbon	500	1.5	24.3	0.20	(69)
Graphene aerogel	500	1.2	9.9	0.99	(70)
Graphene sponge	500	1.5	14.9	0.50	(71)
Three-dimensional macroporous graphene	$105 \mu\text{S cm}^{-1}$	1.2	2.0	2.18	(12)
Holey graphene sheet	5000	1.2	26.8	0.45	(13)
Sandwich-like nitrogen-doped graphene composite	500	1.0	10.3	0.19	(72)
3D intercalated graphene sheet-sphere nanocomposite	500	1.2	22.1	0.35	(73)

Porous Carbon

Poly(sulfobetaine methacrylate)-coated porous carbon	245	1.2	16.5	3.3	(74)
--	-----	-----	------	-----	------

Basswood-derived hierarchically porous carbon monoliths	100	1.2	5.7	0.033	(23)
Mesoporous carbon film	23500	1.2	21.0	2.1	(75)
Carbon aerogel	2250	1.3	7.1	0.071	(76)
TiC-derived carbon powder	290	1.2	10.1	1.01	(31)
YP50-F activated carbon	290	1.2	9.1	0.91	(31)
Mesoporous templated carbon	290	1.2	12.8	1.28	(31)
CO ₂ -activated CF/carbon black	90	1.6	9.1	0.075	(47)
Carbide-derived microporous carbon	290	1.4	14.9	0.89	(9)
Carbon aerogel monolith	2922	1.5	9.6	0.96	(48)
Silica-templated ordered mesoporous carbon	500	1.2	10.8	0.06	(77)
N-doped hollow carbon sphere	500	1.4	13.0	0.22	(78)

Loofa-derived porous carbon monolith	585	1.0	22.5	0.38	(15)
Zwitterionic polymer coated porous carbon	245	1.2	16.5	3.3	(74)
N-doped porous carbon spheres	1000	1.2	14.9	0.50	(79)
Biomass-derived N-doped porous carbon	40	1.2	15.5	0.44	(14)
N-doped pollen-derived porous carbon powder	~260	1.4	18.0	0.30	(80)
N-doped mesoporous carbon spheres	584	1.2	20.6	0.67	(36)
Meso-, micro-porous activated carbon powder	584	1.0	20.9	0.35	(81)
N-doped carbon sheet/rGO composite	589	1.2	17.5	1.75	(82)
Ordered mesoporous carbon nano-polyhedra	584	1.2	14.6	0.49	(20)
Polypyrrole-derived nano-porous carbon sheet	1169	1.2	27.4	2.5	(83)

Activated carbon (MSP-20)	292	1.2	15.2	0.59	(84)
H ₂ -treated carbon beads	292	1.2	11.6	1.2	(84)
H ₂ -treated carbon beads	292	1.2	10.7	2.4	(84)
Activated carbon (YP- 50)	1169	1.2	9.2	0.90	(50)
Activated carbon (YP- 50)	1169	1.2	4.3	2.4	(50)
Metal organic framework-based carbon	584	1.2	6.9	5.4	(85)
Metal organic framework-based carbon	584	1.2	10.7	2.4	(85)
Activated luffa- derived biowaste porous carbon sponge	2500	1.0	25.0	0.42	(86)
N, P, S co-doped hollow carbon polyhedron	500	1.0	14.0	0.12	(87)

^{a)} Acronyms of materials: CNT – carbon nanotube; CNF – carbon nanofiber; PAN – poly(acrylonitrile); rGO – reduced graphene oxide.

REFERENCES AND NOTES

1. M. Rodell, J. S. Famiglietti, D. N. Wiese, J. T. Reager, H. K. Beaudoin, F. W. Landerer, M. H. Lo, Emerging trends in global freshwater availability. *Nature* **557**, 651–659 (2018).
2. H. Y. Yang, Z. J. Han, S. F. Yu, K. L. Pey, K. Ostrikov, R. Karnik, Carbon nanotube membranes with ultrahigh specific adsorption capacity for water desalination and purification. *Nat. Commun.* **4**, 2220 (2013).
3. Z. S. Cao, S. Zeng, Z. Xu, A. Arvanitis, S. Yang, X. Gu, J. Dong, Ultrathin ZSM-5 zeolite nanosheet laminated membrane for high-flux desalination of concentrated brines. *Sci. Adv.* **4**, eaau8634 (2018).
4. S. Porada, R. Zhao, A. van der Wal, V. Presser, P. M. Biesheuvel, Review on the science and technology of water desalination by capacitive deionization. *Prog. Mater. Sci.* **58**, 1388–1442 (2013).
5. L. Wang, J. E. Dykstra, S. Lin, Energy efficiency of capacitive deionization. *Environ. Sci. Technol.* **53**, 3366–3378 (2019).
6. B. W. Byles, D. A. Cullen, K. L. More, E. Pomerantseva, Tunnel structured manganese oxide nanowires as redox active electrodes for hybrid capacitive deionization. *Nano Energy* **44**, 476–488 (2018).
7. Z. Y. Leong, G. Lu, H. Y. Yang, Three-dimensional graphene oxide and polyvinyl alcohol composites as structured activated carbons for capacitive desalination. *Desalination* **451**, 172–181 (2019).
8. Z.-H. Huang, Z. Yang, F. Kang, M. Inagaki, Carbon electrodes for capacitive deionization. *J. Mater. Chem. A* **5**, 470–496 (2017).
9. S. Porada, L. Weinstein, R. Dash, A. van der Wal, M. Bryjak, Y. Gogotsi, P. M. Biesheuvel, Water desalination using capacitive deionization with microporous carbon electrodes. *ACS Appl. Mater. Interfaces* **4**, 1194–1199 (2012).

10. C.-H. Hou, C.-Y. Huang, A comparative study of electrosorption selectivity of ions by activated carbon electrodes in capacitive deionization. *Desalination* **314**, 124–129 (2013).
11. H. Li, T. Lu, L. Pan, Y. Zhang, Z. Sun, Electrosorption behavior of graphene in NaCl solutions. *J. Mater. Chem.* **19**, 6773–6779 (2009).
12. H. Wang, D. Zhang, T. Yan, X. Wen, J. Zhang, L. Shi, Q. Zhong, Three-dimensional macroporous graphene architectures as high performance electrodes for capacitive deionization. *J. Mater. Chem. A* **1**, 11778–11789 (2013).
13. W. Kong, X. Duan, Y. Ge, H. Liu, J. Hu, X. Duan, Holey graphene hydrogel with in-plane pores for high-performance capacitive desalination. *Nano Res.* **9**, 2458–2466 (2016).
14. C. Zhao, G. Liu, N. Sun, X. Zhang, G. Wang, Y. Zhang, H. Zhang, H. Zhao, Biomass-derived N-doped porous carbon as electrode materials for Zn-air battery powered capacitive deionization. *Chem. Eng. J.* **334**, 1270–1280 (2018).
15. C. Feng, Y.-A. Chen, C.-P. Yu, C.-H. Hou, Highly porous activated carbon with multi-channeled structure derived from loofa sponge as a capacitive electrode material for the deionization of brackish water. *Chemosphere* **208**, 285–293 (2018).
16. A. Omosebi, X. Gao, J. Rentschler, J. Landon, K. Liu, Continuous operation of membrane capacitive deionization cells assembled with dissimilar potential of zero charge electrode pairs. *J. Colloid Interface Sci.* **446**, 345–351 (2015).
17. A. C. Forse, J. M. Griffin, C. Merlet, J. Carretero-Gonzalez, A.-R. O. Raji, N. M. Trease, C. P. Grey, Direct observation of ion dynamics in supercapacitor electrodes using in situ diffusion NMR spectroscopy. *Nat. Energy* **2**, 16216 (2017).
18. F. Zhang, T. Liu, M. Li, M. Yu, Y. Luo, Y. Tong, Y. Li, Multiscale pore network boosts capacitance of carbon electrodes for ultrafast charging. *Nano Lett.* **17**, 3097–3104 (2017).

19. C. Péan, C. Merlet, B. Rotenberg, P. A. Madden, P.-L. Taberna, B. Daffos, M. Salanne, P. Simon, On the dynamics of charging in nanoporous carbon-based supercapacitors. *ACS Nano* **8**, 1576–1583 (2014).
20. X. Xu, H. Tan, Z. Wang, C. Wang, L. Pan, Y. V. Kaneti, T. Yang, Y. Yamauchi, Extraordinary capacitive deionization performance of highly-ordered mesoporous carbon nano-polyhedra for brackish water desalination. *Environ. Sci. Nano* **6**, 981–989 (2019).
21. Z. Zhou, T. Liu, A. U. Khan, G. Liu, Block copolymer-based porous carbon fibers. *Sci. Adv.* **5**, eaau6852 (2019).
22. X. Wen, D. Zhang, L. Shi, T. Yan, H. Wang, J. Zhang, Three-dimensional hierarchical porous carbon with a bimodal pore arrangement for capacitive deionization. *J. Mater. Chem.* **22**, 23835–23844 (2012).
23. M. Liu, M. Xu, Y. Xue, W. Ni, S. Huo, L. Wu, Z. Yang, Y.-M. Yan, Efficient capacitive deionization using natural basswood-derived, freestanding, hierarchically porous carbon electrodes. *ACS Appl. Mater. Interfaces* **10**, 31260–31270 (2018).
24. X. Xu, Z. Sun, D. H. C. Chua, L. Pan, Novel nitrogen doped graphene sponge with ultrahigh capacitive deionization performance. *Sci. Rep.* **5**, 11225 (2015).
25. Z. Zhou, G. Liu, Controlling the pore size of mesoporous carbon thin films through thermal and solvent annealing. *Small* **13**, 1603107 (2017).
26. T. Liu, Z. Zhou, Y. Guo, D. Guo, G. Liu, Block copolymer derived uniform mesopores enable ultrafast electron and ion transport at high mass loadings. *Nat. Commun.* **10**, 675 (2019).
27. K. S. W. Sing, D. H. Everett, R. A. W. Haul, L. Moscou, R. A. Pierotti, J. Rouquérol, T. Siemieniewska, Reporting physisorption data for gas/solid systems with special reference to the determination of surface area and porosity. *Pure Appl. Chem.* **57**, 603 (1985).

28. S. M. Khan, H. Kitayama, Y. Yamada, S. Gohda, H. Ono, D. Umeda, K. Abe, K. Hata, T. Ohba, High CO₂ sensitivity and reversibility on nitrogen-containing polymer by remarkable CO₂ adsorption on nitrogen sites. *J. Phys. Chem. C* **122**, 24143–24149 (2018).
29. F. Stoeckli, T. A. Centeno, On the determination of surface areas in activated carbons. *Carbon* **43**, 1184–1190 (2005).
30. M. Thommes, K. Kaneko, A. V. Neimark, J. P. Olivier, F. Rodriguez-Reinoso, J. Rouquerol, K. S. W. Sing, Physisorption of gases, with special reference to the evaluation of surface area and pore size distribution (IUPAC Technical Report). *Pure Appl. Chem.* **87**, 1051–1069 (2015).
31. S. Porada, L. Borchardt, M. Oschatz, M. Bryjak, J. S. Atchison, K. J. Keesman, S. Kaskel, P. M. Biesheuvel, V. Presser, Direct prediction of the desalination performance of porous carbon electrodes for capacitive deionization. *Energ. Environ. Sci.* **6**, 3700–3712 (2013).
32. T. Liu, F. Zhang, Y. Song, Y. Li, Revitalizing carbon supercapacitor electrodes with hierarchical porous structures. *J. Mater. Chem. A* **5**, 17705–17733 (2017).
33. L. Li, L. Zou, H. Song, G. Morri, Ordered mesoporous carbons synthesized by a modified sol–gel process for electrosorptive removal of sodium chloride. *Carbon* **47**, 775–781 (2009).
34. M. S. A. Rahaman, A. F. Ismail, A. Mustafa, A review of heat treatment on polyacrylonitrile fiber. *Polym. Degrad. Stab.* **92**, 1421–1432 (2007).
35. J.-S. Wei, C. Ding, P. Zhang, H. Ding, X.-Q. Niu, Y.-Y. Ma, C. Li, Y.-G. Wang, H.-M. Xiong, Robust negative electrode materials derived from carbon dots and porous hydrogels for high-performance hybrid supercapacitors. *Adv. Mater.* **31**, 1806197 (2019).
36. X. Xu, A. E. Allah, C. Wang, H. Tan, A. A. Farghali, M. H. Khedr, V. Malgras, T. Yang, Y. Yamauchi, Capacitive deionization using nitrogen-doped mesostructured carbons for highly efficient brackish water desalination. *Chem. Eng. J.* **362**, 887–896 (2019).
37. P. Rani, V. K. Jindal, Designing band gap of graphene by B and N dopant atoms. *RSC Adv.* **3**, 802–812 (2013).

38. H. Su, H. Huang, H. Zhang, X. Chu, B. Zhang, B. Gu, X. Zheng, S. Wu, W. He, C. Yan, J. Chen, W. Yang, In situ direct method to massively prepare hydrophilic porous carbide-derived carbons for high-performance supercapacitors. *ACS Appl. Energy Mater.* **1**, 3544–3553 (2018).
39. P. M. Biesheuvel, S. Porada, M. Levi, M. Z. Bazant, Attractive forces in microporous carbon electrodes for capacitive deionization. *J. Solid State Electrochem.* **18**, 1365–1376 (2014).
40. Y. T. Qu, P. G. Campbell, L. Gu, J. M. Knipe, E. Dzenitis, J. G. Santiago, M. Stadermann, Energy consumption analysis of constant voltage and constant current operations in capacitive deionization. *Desalination* **400**, 18–24 (2016).
41. J. E. Dykstra, S. Porada, A. van der Wal, P. M. Biesheuvel, Energy consumption in capacitive deionization—Constant current versus constant voltage operation. *Water Res.* **143**, 367–375 (2018).
42. Y. Marcus, Ionic radii in aqueous solutions. *Chem. Rev.* **88**, 1475–1498 (1988).
43. J. M. Serrano, T. Liu, A. U. Khan, B. Botset, B. J. Stovall, Z. Xu, D. Guo, K. Cao, X. Hao, S. Cheng, G. Liu, Composition design of block copolymers for porous carbon fibers. *Chem. Mater.* **31**, 8898–8907 (2019).
44. Z. Zhou, T. Liu, A. U. Khan, G. Liu, Controlling the physical and electrochemical properties of block copolymer-based porous carbon fibers by pyrolysis temperature. *Mol. Syst. Des. Eng.* **5**, 153–165 (2020).
45. H. Li, Y. Gao, L. Pan, Y. Zhang, Y. Chen, Z. Sun, Electrosorptive desalination by carbon nanotubes and nanofibres electrodes and ion-exchange membranes. *Water Res.* **42**, 4923–4928 (2008).
46. J. Kamcev, D. R. Paul, B. D. Freeman, Equilibrium ion partitioning between aqueous salt solutions and inhomogeneous ion exchange membranes. *Desalination* **446**, 31–41 (2018).
47. G. Wang, Q. Dong, Z. Ling, C. Pan, C. Yu, J. Qiu, Hierarchical activated carbon nanofiber webs with tuned structure fabricated by electrospinning for capacitive deionization. *J. Mater. Chem.* **22**, 21819–21823 (2012).

48. M. E. Suss, T. F. Baumann, W. L. Bourcier, C. M. Spadaccini, K. A. Rose, J. G. Santiago, M. Stadermann, Capacitive desalination with flow-through electrodes. *Energ. Environ. Sci.* **5**, 9511–9519 (2012).
49. D. Qu, G. Wang, J. Kafle, J. Harris, L. Crain, Z. Jin, D. Zheng, Electrochemical impedance and its applications in energy-storage systems. *Small Methods* **2**, 1700342 (2018).
50. T. Kim, J. E. Dykstra, S. Porada, A. van der Wal, J. Yoon, P. M. Biesheuvel, Enhanced charge efficiency and reduced energy use in capacitive deionization by increasing the discharge voltage. *J. Colloid Interface Sci.* **446**, 317–326 (2015).
51. F. Ehrburger-Dolle, M. Holz, J. Lahaye, Use of N₂, Ar and CO₂ adsorption for the determination of microporosity and surface fractal dimension of carbon blacks and silicas. *Pure Appl. Chem.* **65**, 2223–2230 (1993).
52. K. C. Kim, T.-U. Yoon, Y.-S. Bae, Applicability of using CO₂ adsorption isotherms to determine BET surface areas of microporous materials. *Micropor. Mesopor. Mat.* **224**, 294–301 (2016).
53. H. Li, L. Pan, Y. Zhang, L. Zou, C. Sun, Y. Zhan, Z. Sun, Kinetics and thermodynamics study for electrosorption of NaCl onto carbon nanotubes and carbon nanofibers electrodes. *Chem. Phys. Lett.* **485**, 161–166 (2010).
54. L. Wang, M. Wang, Z.-H. Huang, T. Cui, X. Gui, F. Kang, K. Wang, D. Wu, Capacitive deionization of NaCl solutions using carbon nanotube sponge electrodes. *J. Mater. Chem. A* **21**, 18295–18299 (2011).
55. A. Aldalbahi, M. Rahaman, M. Almoiqli, A. Hamedelniel, A. Alrehaili, Single-walled carbon nanotube (SWCNT) loaded porous reticulated vitreous carbon (RVC) electrodes used in a capacitive deionization (CDI) cell for effective desalination. *Nanomaterials* **8**, 527 (2018).
56. X. Xu, Y. Liu, T. Lu, Z. Sun, D. H. C. Chua, L. Pan, Rational design and fabrication of graphene/carbon nanotubes hybrid sponge for high-performance capacitive deionization. *J. Mater. Chem. A* **3**, 13418–13425 (2015).

57. S. Wang, D. Z. Wang, L. J. Ji, Q. Gong, Y. F. Zhu, J. Liang, Equilibrium and kinetic studies on the removal of NaCl from aqueous solutions by electrosorption on carbon nanotube electrodes. *Sep. Purif. Technol.* **58**, 12–16 (2007).
58. M. Wang, Z.-H. Huang, L. Wang, M.-X. Wang, F. Kang, H. Hou, Electrospun ultrafine carbon fiber webs for electrochemical capacitive desalination. *New J. Chem.* **34**, 1843–1845 (2010).
59. J. Liu, S. Wang, J. Yang, J. Liao, M. Lu, H. Pan, L. An, ZnCl₂ activated electrospun carbon nanofiber for capacitive desalination. *Desalination* **344**, 446–453 (2014).
60. A. G. El-Deen, N. A. M. Barakat, K. A. Khalil, H. Y. Kim, Hollow carbon nanofibers as an effective electrode for brackish water desalination using the capacitive deionization process. *New J. Chem.* **38**, 198–205 (2014).
61. Y. Belaustegui, S. Zorita, F. Fernández-Carretero, A. García-Luis, F. Pantò, S. Stelitano, P. Frontera, P. Antonucci, S. Santangelo, Electro-spun graphene-enriched carbon fibres with high nitrogen-contents for electrochemical water desalination. *Desalination* **428**, 40–49 (2018).
62. G. Zhu, H. Wang, H. Xu, L. Zhang, Enhanced capacitive deionization by nitrogen-doped porous carbon nanofiber aerogel derived from bacterial-cellulose. *J. Electroanal. Chem.* **822**, 81–88 (2018).
63. Y. Li, Y. Liu, M. Wang, X. Xu, T. Lu, C. Q. Sun, L. Pan, Phosphorus-doped 3D carbon nanofiber aerogels derived from bacterial-cellulose for highly-efficient capacitive deionization. *Carbon* **130**, 377–383 (2018).
64. N. Pugazhenthiran, S. Sen Gupta, A. Prabhath, M. Manikandan, J. R. Swathy, V. K. Raman, T. Pradeep, Cellulose derived graphenic fibers for capacitive desalination of brackish water. *ACS Appl. Mater. Interfaces* **7**, 20156–20163 (2015).
65. W. Shi, H. Li, X. Cao, Z. Y. Leong, J. Zhang, T. Chen, H. Zhang, H. Y. Yang, Ultrahigh performance of novel capacitive deionization electrodes based on a three-dimensional graphene architecture with nanopores. *Sci. Rep.* **6**, 18966 (2016).

66. X. Wen, D. Zhang, T. Yan, J. Zhang, L. Shi, Three-dimensional graphene-based hierarchically porous carbon composites prepared by a dual-template strategy for capacitive deionization. *J. Mater. Chem. A* **1**, 12334–12344 (2013).
67. X. Xu, L. Pan, Y. Liu, T. Lu, Z. Sun, Enhanced capacitive deionization performance of graphene by nitrogen doping. *J. Colloid Interface Sci.* **445**, 143–150 (2015).
68. H. Wang, L. Shi, T. Yan, J. Zhang, Q. Zhong, D. Zhang, Design of graphene-coated hollow mesoporous carbon spheres as high performance electrodes for capacitive deionization. *J. Mater. Chem. A* **2**, 4739–4750 (2014).
69. O. Noonan, Y. Liu, X. Huang, C. Yu, Layered graphene/mesoporous carbon heterostructures with improved mesopore accessibility for high performance capacitive deionization. *J. Mater. Chem. A* **6**, 14272–14280 (2018).
70. H. Yin, S. Zhao, J. Wan, H. Tang, L. Chang, L. He, H. Zhao, Y. Gao, Z. Tang, Three-dimensional graphene/metal oxide nanoparticle hybrids for high-performance capacitive deionization of saline water. *Adv. Mater.* **25**, 6270–6276 (2013).
71. X. Xu, L. Pan, Y. Liu, T. Lu, Z. Sun, D. H. C. Chua, Facile synthesis of novel graphene sponge for high performance capacitive deionization. *Sci. Rep.* **5**, 8458 (2015).
72. T. Yan, J. Liu, H. Lei, L. Shi, Z. An, H. S. Park, D. Zhang, Capacitive deionization of saline water using sandwich-like nitrogen-doped graphene composites via a self-assembling strategy. *Environ. Sci. Nano* **5**, 2722–2730 (2018).
73. Z. U. Khan, T. Yan, L. Shi, D. Zhang, Improved capacitive deionization by using 3D intercalated graphene sheet–sphere nanocomposite architectures. *Environ. Sci. Nano* **5**, 980–991 (2018).
74. P. Zhang, P. A. Fritz, K. Schroën, H. Duan, R. M. Boom, M. B. Chan-Park, Zwitterionic polymer modified porous carbon for high-performance and antifouling capacitive desalination. *ACS Appl. Mater. Interfaces* **10**, 33564–33573 (2018).

75. C. Tsouris, R. Mayes, J. Kiggans, K. Sharma, S. Yiacoumi, D. DePaoli, S. Dai, Mesoporous carbon for capacitive deionization of saline water. *Environ. Sci. Technol.* **45**, 10243–10249 (2011).
76. P. Xu, J. E. Drewes, D. Heil, G. Wang, Treatment of brackish produced water using carbon aerogel-based capacitive deionization technology. *Water Res.* **42**, 2605–2617 (2008).
77. Z. Chen, H. Zhang, C. Wu, L. Luo, C. Wang, S. Huang, H. Xu, A study of the effect of carbon characteristics on capacitive deionization (CDI) performance. *Desalination* **433**, 68–74 (2018).
78. S. Zhao, T. Yan, H. Wang, G. Chen, L. Huang, J. Zhang, L. Shi, D. Zhang, High capacity and high rate capability of nitrogen-doped porous hollow carbon spheres for capacitive deionization. *Appl. Surf. Sci.* **369**, 460–469 (2016).
79. Y. Liu, T. Chen, T. Lu, Z. Sun, D. H. C. Chua, L. Pan, Nitrogen-doped porous carbon spheres for highly efficient capacitive deionization. *Electrochim. Acta* **158**, 403–409 (2015).
80. Q. Liu, X. Li, Y. Wu, M. Qing, G. Tan, D. Xiao, Pine pollen derived porous carbon with efficient capacitive deionization performance. *Electrochim. Acta* **298**, 360–371 (2019).
81. C.-L. Yeh, H.-C. Hsi, K.-C. Li, C.-H. Hou, Improved performance in capacitive deionization of activated carbon electrodes with a tunable mesopore and micropore ratio. *Desalination* **367**, 60–68 (2015).
82. M. Wang, X. Xu, J. Tang, S. Hou, M. S. A. Hossain, L. Pan, Y. Yamauchi, High performance capacitive deionization electrodes based on ultrathin nitrogen-doped carbon/graphene nano-sandwiches. *Chem. Commun.* **53**, 10784–10787 (2017).
83. F. Ji, L. Wang, J. Yang, X. Wu, M. Li, S. Jiang, S. Lin, Z. Chen, Highly compact, free-standing porous electrodes from polymer-derived nanoporous carbons for efficient electrochemical capacitive deionization. *J. Mater. Chem. A* **7**, 1768–1778 (2019).
84. B. Krüner, P. Srimuk, S. Fleischmann, M. Zeiger, A. Schreiber, M. Aslan, A. Quade, V. Presser, Hydrogen-treated, sub-micrometer carbon beads for fast capacitive deionization with high performance stability. *Carbon* **117**, 46–54 (2017).

85. T. Kim, J. Yoon, CDI ragone plot as a functional tool to evaluate desalination performance in capacitive deionization. *RSC Adv.* **5**, 1456–1461 (2015).
86. D. Sriramulu, S. Vafakhah, H. Y. Yang, Activated *Luffa* derived biowaste carbon for enhanced desalination performance in brackish water. *RSC Adv.* **9**, 14884–14892 (2019).
87. J. Zhang, J. Fang, J. Han, T. Yan, L. Shi, D. Zhang, N, P, S co-doped hollow carbon polyhedra derived from MOF-based core–shell nanocomposites for capacitive deionization. *J. Mater. Chem. A* **6**, 15245–15252 (2018).